euspen's 26th International Conference & Exhibition, Krakow, PL, June 2026
www.euspen.eu

Pore-aware dwell map construction from in-situ pad-glass contact imaging in optical polishing

Nico Zettler[1], Adam Wilczek[1], Prof. Dr. Rainer Börret[1]

[1]*Aalen University, Center for Optical Technologies (ZOT), Beethovenstr. 1, 73430 Aalen, Germany*

nico.zettler@hs-aalen.de

Abstract
Conventional dwell maps in optical polishing assume smooth tool influence functions that ignore the porous structure of real pads. We present an in-situ imaging method that constructs pore-resolved dwell maps directly from measured pad-surface contact, without prior TIF assumptions. Using a telecentric sub-surface imaging setup (5 MP, 12 fps) during force-controlled polishing of N-BK7 substrates (10 N, 830 rpm, ABB IRB 2400 robot), we extract continuous contact intensity maps and accumulate them over time. Radial averaging of each frame's contact intensity captures both the pad's radial contact heterogeneity and velocity variation ($v = \omega \times r$) in a single processing step. Validation against white-light interferometry (nine experiments, two substrates) using leave-one-out cross-validation shows that the pore-aware model ($R^2 = 0.908$) significantly outperforms a uniform topography-free baseline ($R^2 = 0.885, \mathrm{p} = 0.004$). With drift and edge corrections, the full pore-aware model achieves $R^2 = 0.930 \pm 0.033$. The method enables direct observation of pad microstructure effects on material removal and provides a foundation for improved process modelling in deterministic optical fabrication.

optical polishing, dwell map, tool influence function, in-situ monitoring, image processing, material removal prediction

1. Introduction

Computer-controlled optical surfacing (CCOS) is widely used for deterministic fabrication of precision optics and has been a subject of extensive research in optical manufacturing [1,2]. These processes rely on accurate dwell time maps that specify how long the polishing tool must remain at each position to achieve the desired material removal distribution. The relationship between dwell time and removal is governed by the tool influence function (TIF), which describes the spatial distribution of material removal rate beneath the polishing tool [3].

According to the Preston equation, the local material removal rate is proportional to the product of contact pressure and relative velocity [4]. In practice, TIFs are often modeled using smooth, parametric functions such as Gaussian-like profiles, which approximate the spatial distribution of material removal as a function of local contact conditions and tool kinematics [5, 6]. For bonnet polishing, finite element analysis combined with Preston's law has been shown to predict near-Gaussian TIF shapes that agree well with experimental spot tests [7].

However, real polishing pads exhibit porous, heterogeneous microstructures that deviate substantially from these idealized models. Polyurethane pads contain distributed pores that create spatially varying contact conditions at the pad-workpiece interface [8]. While the effect of pad porosity, asperity distribution, and mechanical pad properties on macroscopic material removal rates has been investigated in several experimental studies [9-11], conventional TIF models do not resolve the pad microstructure. The mismatch between assumed smooth contact and actual pore-scale variations may limit the accuracy of deterministic polishing, particularly when pixel-level prediction is required.

Several approaches exist to characterize TIFs experimentally, including spot polishing tests [12] and interferometric removal measurements that provide high-resolution surface topography and removal maps before and after polishing [13]. Recent work has also demonstrated in-situ monitoring approaches for polishing pad surface shape or pad–workpiece interaction during the polishing process [14,2], as well as sensor-based process monitoring combined with machine learning for material removal prediction [15]. However, these methods remain indirect, as they infer the influence function from observed removal rather than measuring the underlying contact distribution directly. To our knowledge, no method has been reported that extracts pore-resolved contact maps from in-situ imaging during the polishing process.

In this work, we present an imaging-based method that constructs pore-resolved dwell maps directly from measured pad-surface contact, without assuming a parametric TIF shape. Using a telecentric camera mounted beneath transparent N-BK7 substrates, we capture the pad-glass interface during polishing and extract continuous contact intensity maps that preserve the pad's porous microstructure. By radially averaging and accumulating these maps over time, we obtain dwell maps that can be validated against interferometrically measured material removal. We demonstrate the method on nine polishing experiments across two optical substrates, achieving $R^2 = 0.930 \pm 0.033$ for the full pore-aware model, significantly outperforming a uniform topography-free baseline at pixel resolution using leave-one-out cross-validation.

2. Experimental setup

The experimental setup consists of a robotic polishing system with integrated sub-surface imaging capability. An ABB IRB 2400 industrial robot (ABB Ltd., Switzerland) guides a rotating polishing head across flat N-BK7 glass substrates (65 mm diameter). The polishing pad is a porous polyurethane disc (Ø 12 mm) mounted on a pneumatic spindle operating at approximately 830 rpm. The pad follows a meander trajectory with 14 mm path width over five passes per experiment. Each polishing run lasted approximately 90 seconds, yielding peak removal depths of circa 0.8 µm. A constant normal force of 10 N is applied via force control throughout the polishing process. Cerium oxide slurry is supplied continuously to the pad-glass interface.

The key feature of the setup is a telecentric imaging system positioned beneath the transparent substrate. A 5-megapixel monochrome camera (Manta G-504B, Allied Vision) equipped with a telecentric lens captures the pad-glass contact zone from below at approximately 12 frames per second. The imaging system provides a spatial resolution of approximately 43 µm/pixel, sufficient to resolve individual pad pores. Coaxial LED illumination ensures uniform brightness across the field of view. This configuration enables direct observation of the porous pad structure in contact with the glass surface during polishing. Figure 1 illustrates the experimental configuration and exemplary camera images showing the pad microstructure.

Material removal is validated using a Zygo NewView 8300 white-light interferometer (WLI), which measures the surface topography before and after each polishing run with sub-nanometer vertical resolution. The difference map provides the ground-truth material removal distribution for comparison with the image-derived dwell maps.

A total of nine polishing experiments were conducted across two N-BK7 substrates, each comprising a complete polishing trajectory with synchronized image acquisition and subsequent WLI measurement.

3. Methods

Image acquisition and preprocessing. During each polishing run, the telecentric camera captures a continuous image sequence of the pad-glass interface at approximately 12 fps. A background model is computed from the first and last frames of the sequence, when the pad is not actively pressing against the substrate. Each frame is preprocessed by subtracting the background model and applying a circular surface mask that isolates the optical substrate from the surrounding bright ring artifacts.

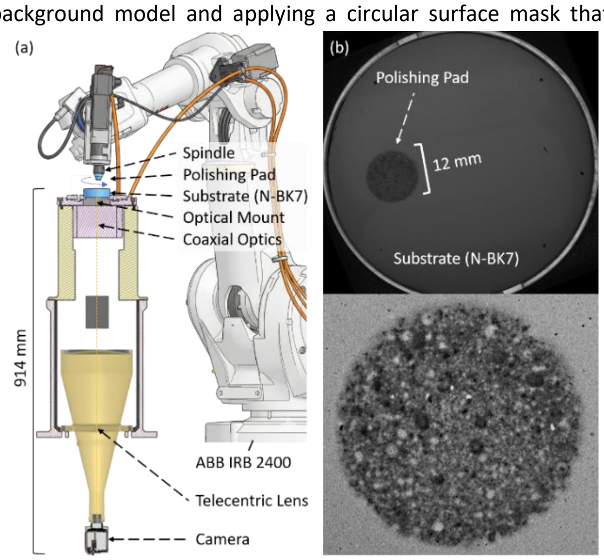

Figure 1. Experimental setup for in-situ pad-glass contact imaging. (a) Schematic showing the ABB robot with polishing head, transparent N-BK7 substrate, and telecentric camera beneath. (b) Top: Raw camera image with polishing pad (ø 12 mm) in contact with the substrate. Bottom: Magnified view revealing the porous pad microstructure, where bright regions indicate pores and dark regions indicate pad-glass contact.

Contact intensity extraction. A calibration step determines the intensity range within detected pad regions across a representative subset of frames. Contact intensity is computed by percentile-based normalization:

$$c(x, y) = \text{clip}\left(\frac{I(x, y) - P_5}{P_{95} - P_5}, 0{,}1\right)$$

where P_5 and P_{95} denote the 5th and 95th percentile of pixel intensities within detected pad regions during calibration. This linear mapping scales the raw intensity to a continuous contact value in [0, 1], where higher values indicate stronger pad-glass contact. The 5th and 95th percentiles provide robust normalization bounds that exclude outliers from specular reflections and sensor noise while preserving the full dynamic range of contact intensities.

Pad detection. For each frame, the pad region is detected using Otsu thresholding on the preprocessed image. The largest connected component is extracted and morphologically filled to obtain a coherent pad mask. The pad center (c_x, c_y) and radius R are determined from the center of mass and equivalent circular area of the detected region.

Pore-aware dwell map construction. The contact maps are accumulated over time to form the pore-aware dwell map D_{pore}. For each pixel location (x, y) on the substrate:

$$D_{pore} = \sum_t c_t(x, y)$$

where the summation runs over all frames in which the pixel falls within the detected pad region. Before accumulation, each frame's contact intensity map is radially averaged with respect to the detected pad center: all pixels at the same radial distance receive the mean intensity of their radial ring. This step captures both the radial contact heterogeneity arising from the pad's porous microstructure and the velocity variation across the pad ($v = \omega \times r$) in a single representation. Figure 2 illustrates this core processing pipeline. The following refinements are applied during model fitting but not visualized, as their parameters are determined through cross-validation.

Registration and validation. An affine transformation registers the image-derived dwell maps to WLI-measured removal maps. Registration parameters were optimized by maximizing normalized cross-correlation in the overlap region. The coefficient of determination (R^2) quantifies the pixel-wise correspondence between predicted dwell and measured removal. A uniform baseline model D_{uni}, which assigns constant intensity (1.0) within the detected pad region and zero outside, serves as a topography-free reference for quantifying the contribution of pad surface information.

Drift correction. Residual analysis revealed systematic spatial trends along the polishing trajectory: predicted removal underestimated the measured removal at the trajectory start and overestimated it towards the end. This gradient is attributed to progressive changes in pad-glass contact visibility during polishing, likely caused by slurry redistribution, pad conditioning, or surface smoothing effects. These trends are modeled by a second-order polynomial surface:

$$D_{drift}(x, y) = \gamma_1 x + \gamma_2 y + \gamma_3 x^2 + \gamma_4 y^2$$

where x, y are normalized pixel coordinates. Second-order terms capture smooth systematic gradients without overfitting to local variations; higher-order polynomials showed no significant improvement in cross-validation.

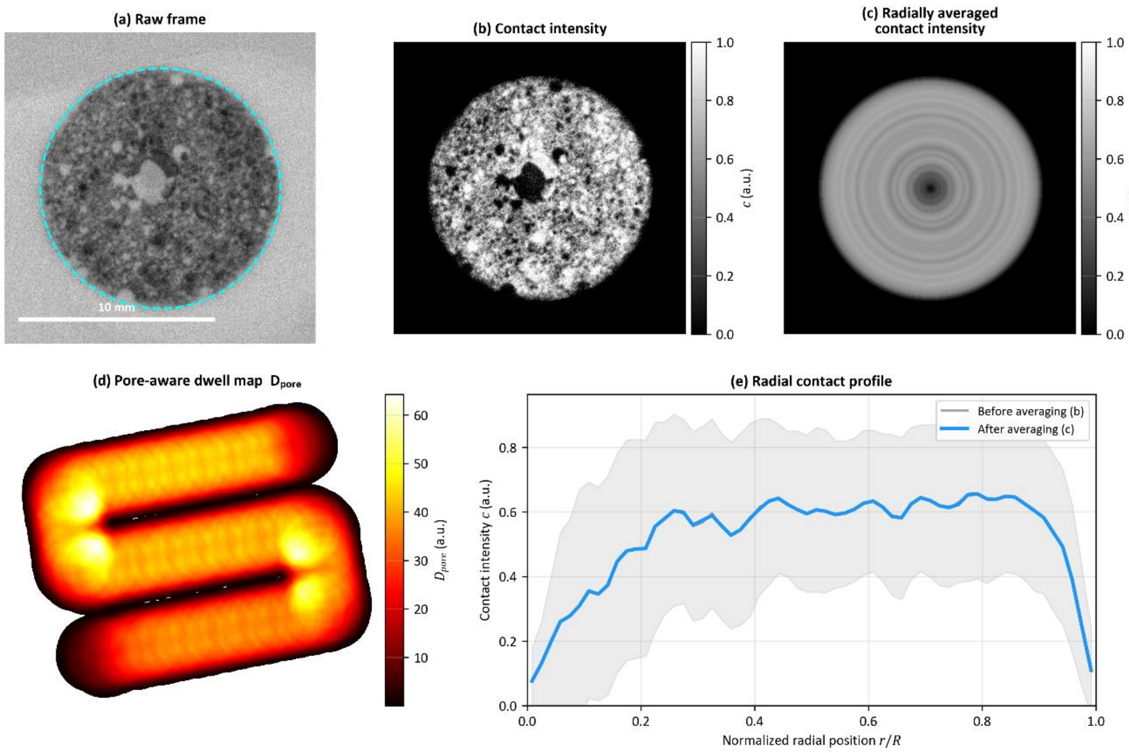

Figure 2. Core processing pipeline for pore-aware dwell map construction. (a) Single video frame with detected pad boundary (dashed circle). (b) Contact intensity after background subtraction and percentile normalization. (c) Radially averaged contact intensity: all pixels at equal radial distance receive the mean intensity of their radial ring. (d) Pore-aware dwell map D_{pore} from temporal accumulation of radially averaged frames. (e) Radial contact profile for a single frame before (gray, showing azimuthal spread) and after (blue). Additional corrections (drift, edge) are applied during model fitting (see Methods). All colorbars in arbitrary units (a.u.).

Edge correction. Contact intensity near the pad boundary is attenuated using a cosine weighting function to account for reduced pressure as the pad transitions on and off the substrate:

$$w\left(\frac{r}{R}\right) = \frac{1}{2}\left(1 + \cos\left(\pi \frac{\left(\frac{r}{R} - r_{cutoff}\right)}{(1 - r_{cutoff})}\right)\right) \text{ for } \frac{r}{R} > r_{cutoff}$$

where r_{cutoff} is optimized on training data. The cosine weighting function was selected empirically from candidate functions (linear, cosine, sigmoid) based on cross-validation performance. The full model combines all components:

$$D_{full} = \alpha \cdot (D_{pore} \cdot w) + D_{drift}$$

The same model structure is applied to the uniform dwell map, yielding $U_{full} = \alpha \cdot (D_{uni} \cdot w) + D_{drift}$, where all parameters are fitted independently.

Cross-validation. Leave-one-out cross-validation (LOOCV) ensures unbiased performance estimates: for each held-out experiment, all parameters (α, γ_1-γ_4, r_{cutoff}) are optimized on the remaining eight experiments and evaluated on the held-out data.

4. Results

Figure 3 shows a representative result from one polishing experiment. The measured removal map (figure 3a) and the predictions from both the pore-aware full model D_{full} (figure 3b) and the uniform full model U_{full} (figure 3c) show close visual agreement. The difference in prediction error (figure 3d) reveals where the pore-aware model improves: it reduces the absolute error in 70% of pixels compared to the uniform model, with the largest improvements concentrated in regions of high cumulative pad contact.

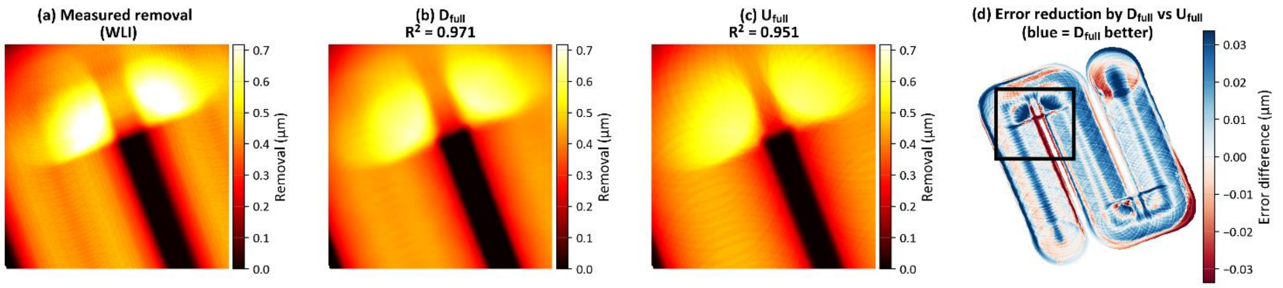

Figure 3. Representative results for one experiment (LOOCV). (a) Measured material removal (WLI), zoomed to region marked in (d). (b) Pore-aware prediction D_{full} ($R^2 = 0.971$). (c) Uniform prediction U_{full} ($R^2 = 0.951$). (d) Prediction error reduction across the full substrate: difference in absolute residuals between U_{full} and D_{full}. Blue indicates regions where the pore-aware model reduces prediction error (70% of pixels). Black rectangle marks the region shown in (a) – (c). Mean performance across all nine experiments is reported in Table 1.

Table 1 summarizes the quantitative results across all nine experiments. Eight model configurations were evaluated using leave-one-out cross-validation, comparing uniform (D_{uni}) and pore-aware (D_{pore}) dwell maps, each with optional drift and edge corrections. The uniform baseline achieves $R^2 = 0.885 \pm 0.038$. The pore-aware model achieves $R^2 = 0.908 \pm 0.039$, a significant improvement ($p = 0.004$, Wilcoxon signed-rank test). This improvement is consistent when corrections are applied: D_{full} ($R^2 = 0.930$) outperforms U_{full} ($R^2 = 0.904$) by $\Delta R^2 = 0.026$ ($p = 0.008$). Notably, the pore-aware model without any corrections ($R^2 = 0.908$) exceeds the uniform baseline with all corrections applied ($R^2 = 0.904$), demonstrating that pad surface information alone provides more predictive value than geometric corrections on a topography-free baseline.

Table 1. Model comparison across nine experiments (LOOCV, mean ± std).

Corrections	D_{uni} (R^2)	D_{pore} (R^2)	ΔR^2
None	0.885 ± 0.038	0.908 ± 0.039	+0.023
Drift	0.893 ± 0.035	0.926 ± 0.033	+0.033
Edge	0.897 ± 0.039	0.915 ± 0.037	+0.018
Drift + Edge	U_{full}: 0.904 ± 0.038	D_{full}: 0.930 ± 0.033	+0.026

5. Discussion and Conclusion

The results demonstrate that pore-resolved dwell maps constructed from in-situ imaging of the pad-glass interface significantly outperform a uniform topography-free baseline. The pore-aware model captures radial contact heterogeneity arising from the pad's porous microstructure, achieving $R^2 = 0.908$ compared to 0.885 for the uniform baseline ($p = 0.004$). With drift and edge corrections, D_{full} achieves $R^2 = 0.930 \pm 0.033$ at pixel resolution using leave-one-out cross-validation.

Radial averaging of each frame's contact intensity captures both the pad's pore-induced contact variation and the velocity gradient ($v = \omega \times r$) in a single predictor, avoiding the need for separate contact and velocity regressors. The improvement over the uniform baseline is consistent across all nine experiments and persists when both models receive identical drift and edge corrections ($\Delta R^2 = +0.026, \mathrm{p} = 0.008$), confirming that the gain originates from pad surface information rather than model complexity. The spatial distribution of the error reduction (figure 3d) supports this interpretation: the largest improvements are concentrated in regions of high cumulative pad contact, where the polishing tool dwells the longest. In these regions, the radial contact profile of the porous pad accumulates over many frames, amplifying the difference between the pore-aware and uniform models. In contrast, regions with short dwell times show smaller differences, as the per-frame contribution of the pore structure is insufficient to produce a measurable effect.

The method offers several advantages over conventional TIF-based approaches. First, it does not require prior calibration through spot polishing tests, as the contact distribution is measured directly during the process. Second, it preserves the spatial heterogeneity of real polishing pads, which smooth TIF models inherently discard. Third, it provides a potential ground-truth reference for validating or refining parametric TIF assumptions. Furthermore, the camera-based approach determines the actual pad position and contact area directly from each frame, avoiding uncertainties inherent in trajectory-based approaches that rely on commanded robot positions. Edge and drift corrections contribute additional improvements for both models, but the pore-aware advantage is maintained across all correction levels (Table 1).

Some limitations remain. The method requires transparent substrates for sub-surface imaging, limiting direct applicability to optical glasses and similar materials. Extension to opaque substrates would require alternative sensing modalities. Process parameters (force, speed, pad type) were held constant across all experiments to isolate model validation from process variability; generalization to other parameter combinations remains for future investigation. Furthermore, the removal rates in this study (0.8 µm in 90 s) represent pre-polishing conditions chosen for measurable signals within practical imaging durations. Validation under finishing conditions with sub-100 nm removal remains for future work. The pore-aware improvement may be more pronounced for larger pad diameters, where radial contact variation spans a wider spatial range, and for variable process conditions, where pad wear and conditioning alter the pore structure over time.

In conclusion, we have presented an imaging-based method for constructing pore-aware dwell maps from in-situ measurements of pad-surface contact during optical polishing. The approach enables direct observation of pad microstructure effects and provides a foundation for improved process modeling in deterministic optical fabrication.

Acknowledgement

This research is part of the "KI-Booster" project (Grant No. P2019-00-043), funded by the Carl Zeiss Foundation, and conducted at Aalen University.

References

[1] Kim D W, Kim S-W and Burge J H 2009 Opt. Express 17 21850–66
[2] Fang F, Zhang X and Weckenmann A 2019 Int. J. Extrem. Manuf. 1 022001
[3] Wang T, Ke X, Huang L, Negi V, Choi H and Kim D W 2024 Light: Adv. Manuf. 5 21
[4] Preston F W 1927 J. Soc. Glass Technol. 11 214–56
[5] Walker D D, Brooks D, King A, Freeman R, Morton R, McCavana G and Kim S-W 2003 Opt. Express 11 958–64
[6] Pan R, Zhang Y, Chen S and Wang Z 2017 Int. J. Mach. Tools Manuf. 118–119 1–11
[7] Li H, Walker D, Yu G and Zhang W 2013 Appl. Opt. 52 5781–87
[8] Prasad A, Fotou G and Li S 2013 J. Mater. Res. 28 2380–93
[9] Thakurta D G, Borst C L, Schwendeman D W, Gutmann R J and Gill W N 2000 Thin Solid Films 366 181–90
[10] Luo J, Dornfeld D and Liang S 2001 IEEE Trans. Semicond. Manuf. 14 112–33
[11] Tseng W-T and Wang Y-L 1999 J. Electrochem. Soc. 146 427–34
[12] Suratwala T, Menapace J, Steele R, Wong L, Tham G, Ray N, Bauman B, Gregory M and Hordin T 2021 Appl. Opt. 60 201–14
[13] de Groot P 2015 Adv. Opt. Technol. 4 301–11
[14] Yin J, Jiao X, Tang W and Zhu J 2018 Opt. Eng. 57 074103
[15] Schneckenburger M, Höfler S, Garcia L, Almeida R and Börret R 2022 SN Appl. Sci. 4 21